ChemPhysChem

Research Article
doi.org/10.1002/cphc.202200031

Chemistry Europe
European Chemical Societies Publishing

www.chemphyschem.org

Direct Visualisation of the Surface Atomic Active Sites of Carbon-Supported Co_3O_4 Nanocrystals via High-Resolution Phase Restoration

Ofentse A. Makgae,*[a, b] Arthur N. Moya,[b] Tumelo N. Phaahlamohlaka,[d, e] Chen Huang,[b, c] Neil J. Coville,[d, e] Angus I. Kirkland,[b, c] and Emanuela Liberti*[b, c]

The atomic arrangement of the terminating facets on spinel Co_3O_4 nanocrystals is strongly linked to their catalytic performance. However, the spinel crystal structure offers multiple possible surface terminations depending on the synthesis. Thus, understanding the terminating surface atomic structure is essential in developing high-performance Co_3O_4 nanocrystals. In this work, we present direct atomic-scale observation of the surface terminations of Co_3O_4 nanoparticles supported on hollow carbon spheres (HCSs) using exit wavefunction reconstruction from aberration-corrected transmission electron microscopy focal-series. The restored high-resolution phases show distinct resolved oxygen and cobalt atomic columns. The data show that the structure of {100}, {110}, and {111} facets of spinel Co_3O_4 exhibit characteristic active sites for carbon monoxide (CO) adsorption, in agreement with density functional theory calculations. Of these facets, the {100} and {110} surface terminations are better suited for CO adsorption than the {111}. However, the presence of oxygen on the {111} surface termination indicates this facet also plays an essential role in CO adsorption. Our results demonstrate direct evidence of the surface termination atomic structure beyond the assumed stoichiometry of the surface.

Introduction

Supported nanostructured spinel cobalt oxide (Co_3O_4) has received attention in heterogeneous catalysis due to its morphology and facet-dependent redox properties.[1–4] Specifically, the catalytic oxidation of carbon monoxide (CO) over supported Co_3O_4 at low temperatures is an environmentally significant catalytic reaction in air pollution remediation from car exhaust emissions.[1,5–8] Facet-dependent reactivity of Co_3O_4 in the low-temperature CO oxidation reaction has been reported for Co_3O_4 nanoparticles,[3] nanorods,[1] nanobelts and nanocubes.[7] Specifically, Xie *et al.*[1] reported a facet-dependent reactivity for Co_3O_4 nanorods in the low-temperature CO oxidation reaction, proposing that {110} facets are more reactive than {111} due to the presence of Co^{3+}. In addition, Hu *et al.*[7] found that Co_3O_4 nanobelts with exposed {110} facets were more active for CO oxidation than nanocubes with predominantly exposed {001} facets. Morphology- and facet-dependent reactivity has also been reported for other Co_3O_4 catalysed reactions.[8–11] This has driven the morphology-tailored synthesis of nanostructured Co_3O_4 with exposed reactive facets for specific reactions.[3]

Co_3O_4 nanocrystals are typically supported on high surface area materials.[3] Of all the supports commonly employed in synthesising supported Co_3O_4 nanocrystals, hollow carbon spheres (HCSs) are attractive due to their precisely controllable particle diameter, shell thickness, surface area and porosity.[12] Unlike oxide supports,[13] they are chemically inert and result in a low metal-support interaction.[14]

Co_3O_4 has a *normal*-spinel crystal structure with an oxygen face centred cubic (fcc) lattice.[15] The Co^{2+} and Co^{3+} cations occupy one-eighth of the tetrahedral interstitial sites and half of the octahedral sites per unit cell, respectively.[15] This complex spinel structure offers multiple possible active catalytic sites depending on the exposed surfaces and the crystal shape. Theoretical studies based on density functional theory (DFT) have shown that the structure of the {111} surfaces results in six possible different terminations, while the {110} surfaces have two possible terminations.[16,17] For low-temperature CO oxidation, DFT shows that facets with Co^{3+} rich terminations result in higher activity than Co^{2+} rich terminations.[18,19] DFT[20–22] calculations also show CO adsorbs more efficiently (adsorption energy −1.18 eV) on a Co^{3+}-O bridge than an octahedral Co^{3+} site (adsorption energy −0.73 eV). Further studies showed that

[a] *Dr. O. A. Makgae*
National Centre for High-Resolution Electron Microscopy, Centre for Analysis and Synthesis, NanoLund, Lund University, Lund 221 00, Sweden
E-mail: ofentse.makgae@chem.lu.se
[b] *Dr. O. A. Makgae, A. N. Moya, Dr. C. Huang, Prof. A. I. Kirkland, Dr. E. Liberti*
Department of Materials, University of Oxford, Parks Roads, Oxford OX1 3PH, United Kingdom
E-mail: emanuela.liberti@rfi.ac.uk
[c] *Dr. C. Huang, Prof. A. I. Kirkland, Dr. E. Liberti*
Electron Physical Science Imaging Centre, Diamond Light Source Ltd., Didcot, OX11 0DE, United Kingdom
[d] *Dr. T. N. Phaahlamohlaka, Prof. N. J. Coville*
DSI-NRF Centre of Excellence in Strong Materials, School of Chemistry, University of the Witwatersrand, Johannesburg 2050, South Africa
[e] *Dr. T. N. Phaahlamohlaka, Prof. N. J. Coville*
Molecular Sciences Institute, School of Chemistry, University of the Witwatersrand, Johannesburg 2050, South Africa

Supporting information for this article is available on the WWW under https://doi.org/10.1002/cphc.202200031

coordinated oxygen at the surface has a significant impact on the catalytic activity of Co_3O_4 during CO oxidation[23–25] because of the Mars-van Krevelen[26]-type mechanism (i.e. the oxidation of CO by oxygen from the lattice, followed by the reoxidation of the catalyst by the oxidant). Furthermore, it has also been shown that oxygen vacancies at the Co_3O_4 (100) surface terminations play an essential role in the oxidation mechanisms of CO at ultra-low temperatures.[27] However, it remains a challenge to document active surface terminations during catalytic reactions because it is difficult to observe such processes directly, *in situ*.[28–30]

Although direct imaging of supported and unsupported Co_3O_4 nanoparticles catalysts has been reported,[15,31–35] however, to date, there is no atomically resolved data showing the oxygen anion surface arrangement, which is generally assumed to be stoichiometric, and the underlying link to CO adsorption. This is mainly because anions are more difficult to image using transmission electron microscopy than cations with stronger contrast. Exit Wavefunction Reconstruction (EWR) recovers the phase of the complex scattered exit wavefunction from a series of aberration-corrected transmission electron microscopy images acquired at different defoci.[36–43]

In this paper, EWR is used to determine the surface atomic structure of Co_3O_4 nanocrystals. The restored phase shows contrast from both Co and O species and can be used to determine the atomic structure at the surface of the Co_3O_4 nanocrystals along several zone axes. These results are then compared with theoretical studies in the literature to identify the active sites for CO adsorption.

Experimental Section

Chemicals

Styrene (Aldrich), polyvinylpyrrolidone (PVP, MW 40 000, Aldrich), cobalt(II) acetate tetrahydrate (Aldrich), benzyl alcohol (Aldrich), ammonia solution (25%; Fluka), potassium persulfate (Eimer and Amend), resorcinol (Aldrich), formaldehyde (Aldrich), hexadecyltrimethylammonium bromide (CTAB; Aldrich), ethanol (98%; Merck), were used as received. Deionised water was used in all experiments.

Synthesis of Hollow Carbon Spheres Supported Co_3O_4 Nanocrystals

Spinel Co_3O_4 nanocrystals were synthesised using a surfactant-free method using cobalt acetate as a precursor salt, benzyl alcohol as the solvent, and ammonia solution as the precipitating agent at 160 °C.[44] Subsequently, HCSs were prepared by coating a spherical polystyrene (PSSs) template with a resorcinol-formaldehyde (RF) polymer to form a composite (PSSs@RF), followed by the decomposition of the template.[45] Finally, the pre-synthesised nanocrystals were loaded on the surface of the HCSs using ethanol as the dispersing solvent in an ultrasonicator.

Aberration-Corrected Focal-Series Exit Wavefunction Reconstruction

High-resolution TEM focal-series images of the Co_3O_4 nanoparticles catalysts were acquired using a double-corrected JEOL ARM-300CF operated at 300 kV using a Gatan OneView camera. Focal-series of 40 images were acquired with a focal step of 1 nm. A 0.4 s exposure time per frame and an image sampling of 0.012 nm/pix were used for all the series (see Table S1 in the supporting information). Each frame of the focal-series was acquired at a total dose of 118840.6 e/nm^2 (see electron dose data in the supporting information). The same electron dose was used for all the experiments. The electron dose was calculated using the calibrated gain of the OneView camera. The complex specimen exit wavefunction was reconstructed *a posteriori* using a linear Weiner filter implemented in the Focal and Tilt Series Reconstruction (FTSR) plugin in the Gatan DigitalMicrograph software.[36] The modulation transfer function (MTF) and the Noise Power Spectrum (NPS) used in the reconstructions were obtained from FTSR.[46]

Care was taken to avoid unnecessarily prolonged beam exposure by tilting the specimen onto a zone axis; instead, only particles that were already suitably oriented were chosen for the focal-series acquisition. Inevitably, some particles were not precisely aligned to a zone axis, resulting in a loss of resolution in the phase (see Figure S2, supporting information), most apparent in thicker regions. Nonetheless, the phase at the particle's surface (which is the area of interest in this study) was atomically resolved.

Total standard error was derived from the combination of statistical, systematic and magnification errors using the Pythagorean theorem. The statistical error was determined from the standard deviation of the average of several measured projected atomic distances extracted from line profiles of surface terminating layers. The systematic error was derived from the average projected atomic distance variation due to a single projected distance measurement change by +/- 1 pixel in the line profile. The magnification error was estimated by comparing the projected spacings at two different magnifications to the projected atomic distance on simulated images. All atomic models used to simulate the TEM data were generated with the CrystalMaker software using the crystallographic data[47] available in the software's database. The specimen exit wavefunction simulations were carried out using the multi-slice algorithm[48] implemented in the MULTEM[49] code (see Table S1 for simulation details in the supporting information)

Results and Discussion

The supported nanocrystals' morphology was initially investigated using conventional bright-field TEM, and a typical image is shown in Figure 1(a). The nanocrystals have a 6.4 nm average size (Figure 1(b)) in the 5–8 nm size range considered optimal for the maximum catalytic activity of CO oxidation.[50] They are supported on the surface of hollow carbon spheres. The latter has a 200 nm diameter and a 25 nm carbon shell thickness (Figure 1(c)). Figure 1 shows that the nanocrystals are well-dispersed and protrude into the vacuum when viewed in projection. This is essential to study the surface at high resolution.

To study the atomic structure of the nanoparticles, the electron beam dose was determined (Figure S3 supporting information) to ensure that sufficient signal-to-noise ratio (S/N) is obtained for the phase of both Co and O atoms with minimal

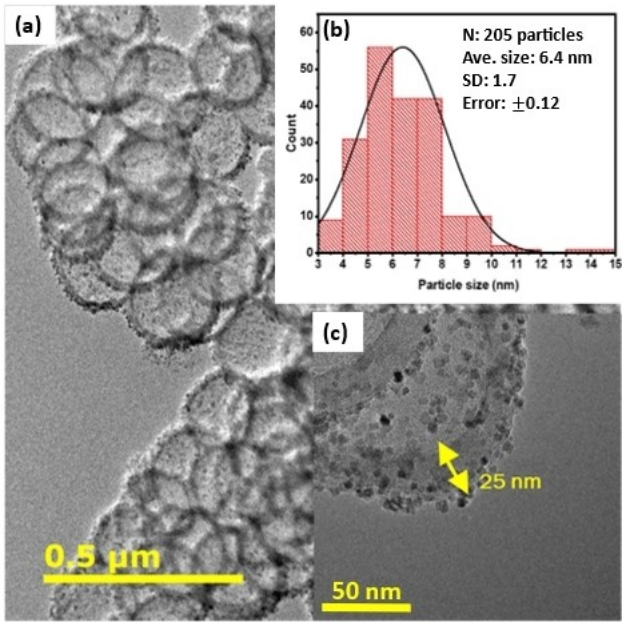

Figure 1. (a) TEM image of Co_3O_4 nanocrystals supported on HCSs. The inset (b) shows the average particle size distribution, and inset (c), bottom shows the 25 nm shell thickness of the HCSs and the well-dispersed nanocrystals at the surface.

beam-induced damage. An electron dose of 118840.6 e/nm^2 per frame (Figure S3 (c)) was used to restore the specimen exit wavefunction from a series of 40 images for all focal series acquisitions. Figure 2(a) illustrates the phase of a nanocrystal with a characteristic spinel Co_3O_4 structure viewed near a $<110>$ zone axis. The near-surface atomic structure qualitatively matches the simulation (Figure 2(c) inset) in the same orientation. Indexing of the square modulus of the complex transform of the exit wavefunction (Figure 2(d)) confirms the $<110>$ projection of the spinel Co_3O_4. The measured projected planar spacing between the octahedral Co atomic columns on the {111} planes is 0.49 nm (±0.039 nm), while the measured projected atomic distance between the tetrahedral Co and O atomic positions on {110} planes is 0.11 nm (±0.009 nm).

The speckled contrast in the vacuum region in Figure 2 is due to noise transferred during the detection process. Although a larger portion of the noise is suppressed in the restoration via the linear Weiner filters, residual noise still transfers to the phase.[37,51] However, at the surface, the phase shift at the oxygen positions is higher than the noise in vacuum (line profile in Figure 2(e)), demonstrating that the oxygen signal is distinguishable from the noise in the speckled region. The nanocrystal in Figure 2(a) has two exposed terminations: a flat {100} and a disordered {110} surface. According to DFT[17] calculations, the {100} surfaces should be either terminated by Co^t_2–$Co^o_4O_8$ or $Co^o_4O_8$–Co^t_2. In this nomenclature, the left side of the hyphen denotes the terminating atomic layer, while the right side is the first subsurface layer. Co^o and Co^t denote octahedral and tetrahedral coordination, respectively, and the subscripts denote (perfect) surface stoichiometry in a unit cell. Of the two possible {100} surface terminations predicted by DFT, the $Co^o_4O_8$–Co^t_2 surface is more thermodynamically stable than the Co^t_2–$Co^o_4O_8$ termination.[17]

In agreement, the {100} surface in Figure 2(b) is terminated by a facet composed of horizontally alternating octahedral Co and O layers ($Co^o_4O_8$–Co^t_2). As mentioned earlier, the presence of coordinated $O_{lattice}$ at the {100} surface positively influences the reactivity of Co_3O_4 by lowering the CO adsorption energy[20–22] and facilitating CO oxidation via the Mars-van-Krevelen[26] type mechanism. Unlike previous imaging studies, which did not resolve O at the surface, the direct visualisation of both O and Co^o at the {100} facet provides strong evidence

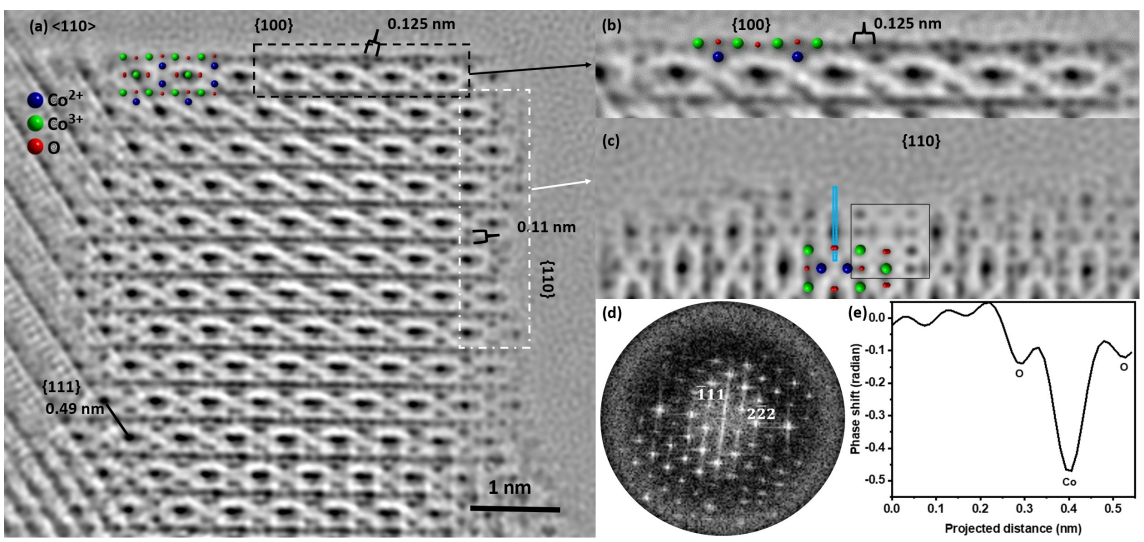

Figure 2. (a) The phase of the restored exit wavefunction of a Co_3O_4 nanocrystal near a $<110>$ zone axis. Atomic column positions are dark (corresponding to a phase advance). (b) Enlarged restored phase of the {100} surface termination in (a) (black dotted box). (c) Enlarged restored phase of the {110} surface termination in (a) (white dotted box). (d) Indexed square modulus of the complex transform of the exit wavefunction in the $<110>$ projection. (e) Line profile from the region marked in blue in (c) showing the O signal is well above noise. Colour-coded atomic models and the simulated phase image are overlaid.

that this surface terminates with the atomic sites that activate the adsorption and dissociation of CO.[22] This information is readily obtained by restoring the phase, but it would be otherwise difficult to obtain from individual HRTEM images, which are not always directly interpretable (supporting information, Figure S5).

Unlike the flat {100} surface, the {110} surface (Figure 2(c)) has a disordered surface termination composed mainly of disordered columns of O and octahedral Co. The line profile in Figure 2(e) confirms that the surface has an O termination, with a higher signal than the vacuum. Equivalent {110} surfaces were also observed along a <111> projection in another Co_3O_4 nanocrystal (Figure 3(a)). The crystallographic phase of the spinel Co_3O_4 in the <111> projection is confirmed by the square modulus of the complex transform of the exit wavefunction (Figure 3(b)). Moreover, the near-surface atomic structure qualitatively matches the simulation (Figure 3(c)–(e) insets) in the same orientation. In this projection, tetrahedral Co atomic columns on {112} planes have a measured planar distance of 0.56 nm (±0.04 nm), while octahedral and tetrahedral Co atomic columns on the {110} planes have an interatomic distance of 0.16 nm (±0.013 nm). The enlarged phase of the {112} surface termination (Figure 3(e)) reveals an atomic layer of octahedral, tetrahedral Co, and O mixed occupancy columns.

DFT[16] studies predict that {110} surfaces are either terminated by $Co^t_2Co^o_2O_4$–$Co^o_2O_4$ or $Co^o_2O_4$–$Co^t_2Co^o_2O_4$ layers, conventionally termed Type A & B, respectively, with the latter being thermodynamically favoured.[17] Our results show that the flat {110} surfaces can have a Type B ($Co^o_2O_4$–$Co^t_2Co^o_2O_4$) surface termination (Figure 3(d)) or a stepped and disordered structure (Figure 2(c) & 3 (c)). Unlike commonly observed steps, where the structure consists of a discontinuation of a single atomic column/layer,[52] critical analysis of the phase reveals a double-step structure (discontinuation of two atomic layers) of Type BAB (Figure 3(c) & (f)). The phase shift associated with the base/terrace atomic column (labelled with a red circle in Figure 3(c)) is larger than at the terrace-terminating atomic column (labelled with a red square in Figure 3(c)), indicating lower atom occupancy at the top of the step. However, the structure of every step at the surface remains the same (as shown by the orange hexagonal regions in Figure 3(c)). This ensures that every terrace in the step is terminated as Type B, consistent with all the observed {110} surface terminations in the nanoparticles. In contrast to the {100} surface, the {110} surface is known to be the most reactive for CO oxidation owing to the presence of a higher density of preferential Co^{3+}–O sites for CO adsorption.[1,7] However, this is only true for surfaces with a Type B termination since Type A contains the inactive tetrahedral Co sites. Our data provide direct experimental evidence that {110} surfaces are highly reactive because they exhibit a Type B termination. In addition, we observe that further enhancement of the reactivity during CO oxidation may be ascribed to a high density of defects, such as steps, in the disordered terminations (Figure 2(c) & 3(c)) depending on the resulting surface energy.[53,54]

An additional equivalent {100} surface was observed in a nanocrystal viewed along a low symmetry <510> zone axis (Figure 4(a)). In this orientation, a {100} $Co^o_4O_8$–Co^t_2 surface termination was found with a projected interatomic spacing of 0.162 nm (±0.013 nm) between adjacent octahedral Co atomic columns. In the equivalent {100} surface termination viewed along a <110> zone axis (Figure 2(b)), adjacent columns have a projected distance of 0.125 nm (±0.01 nm), corresponding to the separation between Co–O columns. Both surfaces (Figure 2(b) and 4(a)) have the same atomic terminating layer.

In addition to {110} terminating facets, the nanocrystal in this orientation also exposes equivalent {115} surfaces. As shown in Figure 4(a), these surfaces are both terminated by a densely packed O, tetrahedral and octahedral Co layer. Such high index surfaces are rarely studied experimentally due to their thermodynamic instability.[17] Consequently, there is also a lack of supporting theoretical studies. To summarise our

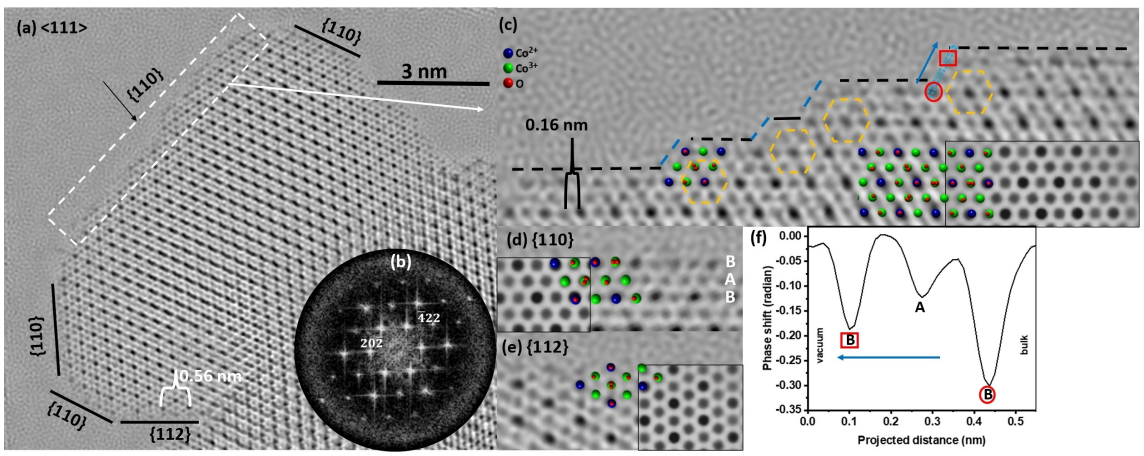

Figure 3. (a) Phase of the restored exit wavefunction of Co_3O_4 projected near a <111> zone axis. The atomic positions are shown as dark. (b) Square modulus of the complex transform of the exit wavefunction in the <111> projection. (c) Enlarged restored phase of the {110} stepped surface of Co_3O_4 from the white dotted box in Figure 3(a). (d) and (e) Enlarged restored phases of the flat {110} and {112} surface terminations of Co_3O_4, respectively. Colour-coded atomic models and the simulated phase are overlaid. (f) The line profile of the step in the surface termination in Figure 3(c) is shown by the blue arrow.

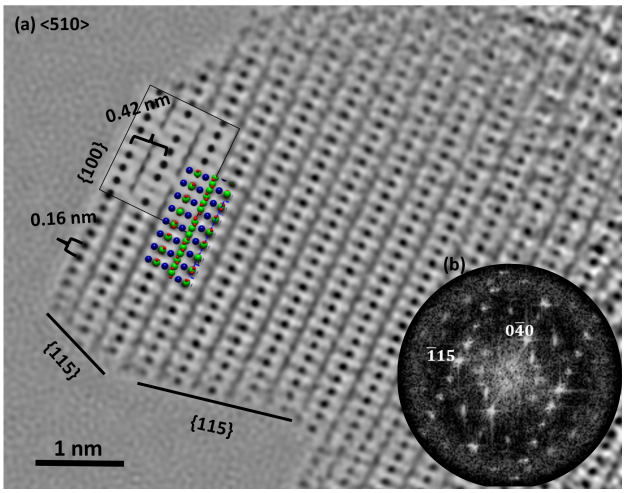

Figure 4. (a) Phase of the exit wavefunction restored from a Co_3O_4 nanoparticle projected near a $<510>$ zone axes. The atomic positions are shown as dark. (b) Square modulus of the complex transform of the exit wavefunction in the $<510>$ projection. Colour-coded atomic models and multi-slice simulations are overlaid.

Table 1. The experimentally observed Co_3O_4 active surface terminations and predicted DFT surface terminations (*denotes the thermodynamically stable terminations calculated using DFT).

Surface	Surface Termination(s) This study	DFT
{100}	$_{<110>}$ $Co^{o}_4O_8$–Co^{t}_2	Co^{t}_2–$Co^{o}_4O_8$ or $Co^{o}_4O_8$–Co^{t}_2*
	$_{<510>}$ $Co^{o}_4O_8$–Co^{t}_2	Ref. [17]
{110}	$_{<110>}$ Rough	Type A ($Co^{t}_2Co^{o}_2O_4$–$Co^{o}_2O_4$)
	$_{<111>}$ Stepped	or Type B ($Co^{o}_2O_4$–$Co^{t}_2Co^{o}_2O_4$)*
	$_{<111>}$ Type B	Ref. [16,17]
	$_{<111>}$ Type B	
	$_{<111>}$ Type B	
{111}	$_{<112>}$ O_4–Co^{t}	O_4–Co^{t}, O_4–Co^{o}_3, Co^{t}–Co^{o}, Co^{t}–O_4, Co^{o}–Co^{t}, Co^{o}_3–O_4 Ref. [17]

findings, Table 1 provides a list of the surface terminations observed by high-resolution phase retrieval, which are also predicted theoretically by DFT studies.

Finally, we report on the restored phase of a Co_3O_4 nanocrystal viewed near a $<112>$ projection (Figure 5). Indexing of the square modulus of the complex transform of the exit wavefunction (Figure 5(c)) confirms the $<112>$ projection of the spinel Co_3O_4. Moreover, the near-surface atomic structure qualitatively matches the simulation (Figure 5(b) & (d) insets) in the same orientation. This nanoparticle has three surfaces: two equivalent {113} surfaces, where one is defective, and a {111} surface. The flat {113} surface is terminated with an octahedral Co layer while the other surface is stepped (Figure 5(b)). Comparing the surface structure with the overlayed atomic model reveals a multi-step structure comprising densely packed oxygen, tetrahedral and octahedral Co atomic columns (steps). The terrace comprises an octahedral Co atomic layer. The structure of the steps remains the same across the surface, as shown by the red dotted lines in Figure 5(b). Flat and defective Co_3O_4 {113} surfaces have been previously observed experimentally;[55] however, there are limited reports describing DFT calculations for possible {113} surface terminations and their reactivity. Nevertheless, as mentioned earlier, defective surfaces are generally more reactive than flat surfaces.[56,57]

The remaining facet observed in the Co_3O_4 nanocrystal in Figure 5(d) shows that the {111} surface is O_4–Co^{t} terminated. This termination is one of possible six for a {111} surface,[17] however, this surface is less active than the {100} and {110} for CO oxidation[1] because of the inactive tetrahedral Co^{2+}. Nevertheless, the presence of oxygen in this termination (O_4–Co^{t}) may still be favourable for CO oxidation via participation in the oxidation cycle according to the Mars-van Krevelen[26] mechanism, as described earlier.

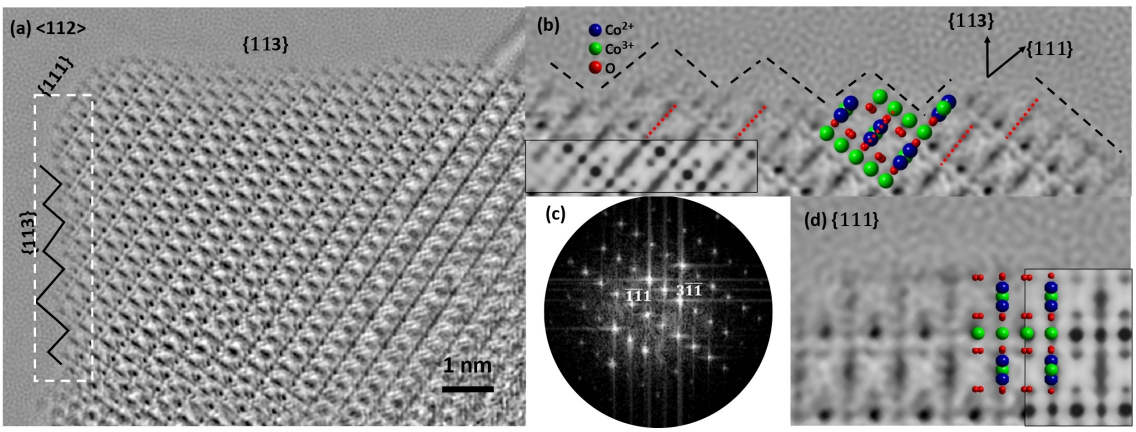

Figure 5. (a) Phase of the restored exit wavefunction of Co_3O_4 projected from a $<112>$ zone axis. The atomic positions are shown as dark. (b) Enlarged restored phase of the {113} stepped surface of Co_3O_4 from the white dotted box in Figure 5(a). (c) Square modulus of the complex transform of the exit wavefunction in the $<112>$ projection. (d) Enlarged restored phase of the {111} surface termination of Co_3O_4. Colour-coded atomic models and the simulated phase are overlaid.

Conclusions

In this paper, exit wavefunctions of Co_3O_4 nanocrystals supported on HCSs were restored using high-resolution TEM focal series. The restored phases were used to determine the atomic structures of the chemically active facets of Co_3O_4 for CO adsorption in several different crystal projections. By directly visualising Co and O atomic columns at the surface, the structure of {100}, {110}, and {111} equivalent surfaces were found to match those predicted theoretically. In particular, we show that the {100} and {110} surfaces have the active sites required for the highest reactivity towards CO activation due to the availability of coordinated surface O atoms to octahedral Co atoms. Furthermore, we show the presence of oxygen at the {111} terminations, suggesting that the {111} surface may also participate in CO adsorption. We also show that in addition to perfectly flat terminations, defective highly reactive surfaces are also present. Overall, these results provide experimental evidence of atomically active sites, thus supporting existing theoretical and catalytic data.

Associated Content

Electronic supplementary information is available. Data available upon request from authors.

Authorship Contribution Statement

OAM- conceptualisation, formal analysis, investigation, writing. ANM- investigation, review & editing. TNP- investigation, review & editing. CH- review & editing. NJC- resources, funding acquisition, review & editing. AIK- supervision, resources, funding acquisition, review & editing. EL- supervision, review & editing.

Notes

The authors declare no competing financial interests.

Acknowledgement

The authors acknowledge the Diamond Light Source (United Kingdom) for access and support using the electron Physical Science Imaging Centre (Instrument E02 and proposals number EM17558 and EM19493).

Conflict of Interest

The authors declare no conflict of interest.

Data Availability Statement

The data that support the findings of this study are available from the corresponding author upon reasonable request.

Keywords: active sites · CO oxidation · exit wavefunction reconstruction · facet termination · spinel cobalt oxide

[1] X. Xie, Y. Li, Z.-Q. Liu, M. Haruta, W. Shen, *Nature* **2009**, *458*, 746–749.
[2] Y. Li, W. Shen, *Chem. Soc. Rev.* **2014**, *43*, 1543–1574.
[3] X. Xie, W. Shen, *Nanoscale* **2009**, *1*, 50–60.
[4] Z. Feng, X. Zhu, J. Yang, K. Zhong, Z. Jiang, Q. Yu, Y. Song, Y. Hua, H. Li, H. Xu, *Appl. Surf. Sci.* **2022**, *578*, 151848.
[5] H. Akimoto, *Science.* **2003**, *302*, 1716–1719.
[6] R. C. Rijkeboer, *Catal. Today* **1991**, *11*, 141–150.
[7] L. Hu, K. Sun, Q. Peng, B. Xu, Y. Li, *Nano Res.* **2010**, *3*, 363–368.
[8] X. Tang, J. Li, J. Hao, *Mater. Res. Bull.* **2008**, *43*, 2912–2918.
[9] L. Hu, Q. Peng, Y. Li, *J. Am. Chem. Soc.* **2008**, *130*, 16136–16137.
[10] Z. Chen, S. Wang, W. Liu, X. Gao, D. Gao, M. Wang, S. Wang, *Appl. Catal. A* **2016**, *525*, 94–102.
[11] J. Xiao, Q. Kuang, S. Yang, F. Xiao, S. Wang, L. Guo, *Sci. Rep.* **2013**, *3*, 1–8.
[12] S. Li, A. Pasc, V. Fierro, A. Celzard, *J. Mater. Chem. A* **2016**, *4*, 12686–12713.
[13] J. Jansson, *J. Catal.* **2000**, *194*, 55–60.
[14] H. Xiong, L. L. Jewell, N. J. Coville, *ACS Catal.* **2015**, *5*, 2640–2658.
[15] R. Yu, L. H. Hu, Z. Y. Cheng, Y. D. Li, H. Q. Ye, J. Zhu, *Phys. Rev. Lett.* **2010**, *105*, 226101.
[16] X.-L. Xu, Z.-H. Chen, Y. Li, W.-K. Chen, J.-Q. Li, *Surf. Sci.* **2009**, *603*, 653–658.
[17] A. Montoya, B. S. Haynes, *Chem. Phys. Lett.* **2011**, *502*, 63–68.
[18] H.-F. Wang, R. Kavanagh, Y.-L. Y. Guo, Y.-L. Y. Guo, G. Lu, P. Hu, *J. Catal.* **2012**, *296*, 110–119.
[19] X.-Y. Pang, C. Liu, D.-C. Li, C.-Q. Lv, G.-C. Wang, *ChemPhysChem* **2013**, *14*, 204–212.
[20] D. E. Jiang, S. Dai, *Phys. Chem. Chem. Phys.* **2011**, *13*, 978–984.
[21] Y.-G. Wang, X.-F. Yang, J. Li, *Chin. J. Catal.* **2016**, *37*, 193–198.
[22] X. Shi, S. L. Bernasek, A. Selloni, *Surf. Sci.* **2018**, *677*, 278–283.
[23] L. Nie, D. Mei, H. Xiong, B. Peng, Z. Ren, X. I. P. Hernandez, A. DeLaRiva, M. Wang, M. H. Engelhard, L. Kovarik, A. K. Datye, Y. Wang, *Science.* **2017**, *358*, 1419–1423.
[24] E. J. Peterson, A. T. DeLaRiva, S. Lin, R. S. Johnson, H. Guo, J. T. Miller, J. H. Kwak, C. H. F. Peden, B. Kiefer, L. F. Allard, F. H. Ribeiro, A. K. Datye, *Nat. Commun.* **2014**, *5*, 1–11.
[25] D. Wu, R. Jia, M. Wen, S. Zhong, Q. Wu, Y. Fu, S. Yu, *Inorg. Chem.* **2020**, *59*, 1218–1226.
[26] P. Mars, D. W. van Krevelen, *Chem. Eng. Sci.* **1954**, *3*, 41–59.
[27] Y. Liu, Y. Peng, M. Naschitzki, S. Gewinner, W. Schöllkopf, H. Kuhlenbeck, R. Pentcheva, B. R. Cuenya, *Angew. Chem.* **2021**, *133*, 16650–16656.
[28] S. B. Vendelbo, C. F. Elkjær, H. Falsig, I. Puspitasari, P. Dona, L. Mele, B. Morana, B. J. Nelissen, R. van Rijn, J. F. Creemer, P. J. Kooyman, S. Helveg, *Nat. Mater.* **2014**, *13*, 884–890.
[29] S. Helveg, C. F. Kisielowski, J. R. Jinschek, P. Specht, G. Yuan, H. Frei, *Micron* **2015**, *68*, 176–185.
[30] P. Broqvist, I. Panas, H. Persson, *J. Catal.* **2002**, *210*, 198–206.
[31] J. H. Warner, M. H. Rümmeli, A. Bachmatiuk, M. Wilson, B. Büchner, *ACS Nano* **2010**, *4*, 470–476.
[32] C. Kisielowski, H. Frei, P. Specht, I. D. Sharp, J. A. Haber, S. Helveg, *Adv. Struct. Chem. Imaging* **2016**, *2*, 13.
[33] F. Zasada, W. Piskorz, P. Stelmachowski, A. Kotarba, J.-F. F. Paul, T. Płociński, K. J. Kurzydłowski, Z. Sojka, *J. Phys. Chem. C* **2011**, *115*, 6423–6432.
[34] L. Liu, Z. Cheng, Y. Li, J. Zhu, R. Yu, *J. Phys. Chem. C* **2020**, *124*, 25790–25795.
[35] Z. Zhang, X. Ke, B. Zhang, J. Deng, Y. Liu, W. Liu, H. Dai, F. R. Chen, M. Sui, *J. Phys. Chem. Lett.* **2020**, *11*, 9913–9919.
[36] R. R. Meyer, A. I. Kirkland, W. O. Saxton, *Ultramicroscopy* **2002**, *92*, 89–109.
[37] A. I. Kirkland, R. R. Meyer, *Microsc. Microanal.* **2004**, *10*, 401–413.
[38] W. O. O. Saxton, *Ultramicroscopy* **1994**, *55*, 171–181.
[39] W. Coene, G. Janssen, M. Op De Beeck, D. Van Dyck, *Phys. Rev. Lett.* **1992**, *69*, 3743–3746.

[40] W. M. J. Coene, A. Thust, M. Op De Beeck, D. Van Dyck, *Ultramicroscopy* **1996**, *64*, 109–135.
[41] H. W. Zandbergen, D. Tang, J. Jansen, R. J. Cava, *Ultramicroscopy* **1996**, *64*, 231–247.
[42] A. Thust, W. M. J. Coene, M. Op de Beeck, D. Van Dyck, *Ultramicroscopy* **1996**, *64*, 211–230.
[43] A. Thust, M. H. F. Overwijk, W. M. J. Coene, M. Lentzen, *Ultramicroscopy* **1996**, *64*, 249–264.
[44] N. Shi, W. Cheng, H. Zhou, T. Fan, M. Niederberger, *Chem. Commun.* **2015**, *51*, 1338–1340.
[45] T. N. Phaahlamohlaka, M. W. Dlamini, D. O. Kumi, R. Forbes, L. L. Jewell, N. J. Coville, *Appl. Catal. A* **2020**, *599*, 117617.
[46] R. R. Meyer, A. Kirkland, *Ultramicroscopy* **1998**, *75*, 23–33.
[47] X. Liu, C. Prewitt, *Phys. Chem. Miner.* **1990**, *17*, 168–172.
[48] E. J. Kirkland, *Advanced Computing in Electron Microscopy*, Springer US, Boston, MA, **2010**.
[49] I. Lobato, D. Van Dyck, *Ultramicroscopy* **2015**, *156*, 9–17.
[50] V. Iablokov, R. Barbosa, G. Pollefeyt, I. Van Driessche, S. Chenakin, N. Kruse, *ACS Catal.* **2015**, *5*, 5714–5718.
[51] C. Huang, *Ultra High Resolution Imaging of Radiation-Sensitive Materials*, D.Phil. thesis, University of Oxford, **2016**.
[52] W. K. Burton, N. Cabrera, F. C. Frank, *Philos. Trans. R. Soc. London* **1951**, *243*, 299–358.
[53] G. A. Somorjai, *Langmuir* **1991**, *7*, 3176–3182.
[54] Y. Cai, J. Xu, Y. Guo, J. Liu, *ACS Catal.* **2019**, *9*, 2558–2567.
[55] H. Zhou, M. Kang, D. Wu, B. Lv, *CrystEngComm* **2016**, *18*, 5456–5462.
[56] J. Lu, J. Song, H. Niu, L. Pan, X. Zhang, L. Wang, J.-J. Zou, *Appl. Surf. Sci.* **2016**, *371*, 61–66.
[57] Y.-C. Zhang, L. Pan, J. Lu, J. Song, Z. Li, X. Zhang, L. Wang, J.-J. Zou, *Appl. Surf. Sci.* **2017**, *401*, 241–247.

Manuscript received: January 13, 2022
Revised manuscript received: March 4, 2022
Accepted manuscript online: April 27, 2022
Version of record online: June 1, 2022